

Ramp Compression of Germanium Dioxide to Extreme Conditions: Phase Transitions in an SiO₂ Analog


D. Kim^{1,*}, I. K. Ocampo¹, R. F. Smith,² F. Coppari,² M. Millot², J. K. Wicks,³ J. R. Rygg,⁴ J. H. Eggert,² and T. S. Duffy¹

¹Department of Geosciences, Princeton University, Princeton, New Jersey 08544, USA

²Lawrence Livermore National Laboratory, Livermore, California 94550, USA

³Department of Earth and Planetary Sciences, Johns Hopkins University, Baltimore, Maryland 21218, USA

⁴Laboratory for Laser Energetics, University of Rochester, Rochester, New York 14623, USA

 (Received 9 September 2022; revised 9 May 2023; accepted 5 June 2023; published 8 September 2023)

The high-pressure (HP) behavior of dioxides is of interest due to their extensive polymorphism and role as analogs for SiO₂, a phase expected to be important in the deep mantles of Earth and terrestrial exoplanets. Here we report on dynamic ramp compression of quartz-type germanium dioxide GeO₂ to stresses up to 882 GPa, a higher peak stress than previous studies by a factor of 5. X-ray diffraction data show that HP-PdF₂-type GeO₂ occurs under ramp loading from 154 to 440 GPa, and this phase persists to higher pressure than predicted by theory. Above 440 GPa, we observe evidence for transformation to a new phase of GeO₂. Based on the diffraction data, the best candidate for this new phase is the cotunnite-type structure which has been predicted to be a stable phase of GeO₂ above 300 GPa. The HP-PdF₂-type and cotunnite-type structures are important phases in a wide range of AX₂ compounds, including SiO₂, at multihundred GPa stresses. Our results demonstrate that ramp compression can be an effective technique for synthesizing and characterizing such phases in oxides. In addition, we show that pulsed x-ray diffraction under ramp compression can be used to examine lower-symmetry phases in oxide materials.

DOI: [10.1103/PhysRevX.13.031025](https://doi.org/10.1103/PhysRevX.13.031025)

Subject Areas: Condensed Matter Physics, Geophysics, Materials Science

I. INTRODUCTION

The high-pressure (HP) behavior of AX₂ compounds is of long-standing interest due to their extensive polymorphism and varied transformation pathways [1]. In particular, GeO₂ has attracted considerable attention as an analog of SiO₂ [2], a major expected oxide component of the interior of terrestrial planets both within and outside the Solar System. SiO₂ undergoes a series of phase transitions from quartz to coesite to stishovite to the CaCl₂-type to seifertite over the pressure range of Earth's crust to the core-mantle boundary. Beyond Earth-mantle conditions, SiO₂ has been experimentally shown to adopt the HP-PdF₂-type (often called pyrite-type) structure at 268 GPa [3]. These progressive phase transitions involve an increase in the coordination number (CN) of Si from 4 (e.g., in quartz)

to 6 (e.g., in stishovite) to 6 or 6 + 2 in the HP-PdF₂ structure. Theoretical studies predict a transition to the post-HP-PdF₂ structure such as a Fe₂P -type structure (CN = 9) to occur around 640 GPa at low temperature [4,5], or to the α-PbCl₂-type structure (cotunnite, CN = 9) at higher temperatures but similar pressures [4–7]. Recently, it was predicted that an R $\bar{3}$ phase of SiO₂ can be formed as an intermediate structure with variable coordination numbers of 6, 8, and 9 at 645–890 GPa [8]. The higher coordinated phases of SiO₂ are potentially important materials in the interiors of large rocky and water-rich extrasolar planets which have a wide range of plausible bulk compositions and higher interior pressure and temperature conditions than Earth [9,10].

At high pressures and temperatures, GeO₂ exhibits a similar phase transition sequence as SiO₂ from argutite [(rutile-type) (*P42/mnm*)] to the CaCl₂-type (*Pnnm*), followed by the α-PbO₂-type (*Pbcn*), and finally a HP-PdF₂-type (*Pa $\bar{3}$*) phase up to 130 GPa [2,11–13]. The lower transformation pressures compared to SiO₂ are related to the larger ionic radius of Ge⁴⁺ relative to Si⁴⁺. No post-HP-PdF₂ phase has been previously observed experimentally.

Structures with the space group *Pa $\bar{3}$* are commonly observed in materials at high pressures including in a number of dioxides (SiO₂ [3], SnO₂ [14], PbO₂ [15], and

*Corresponding author: donghoonkim@korea.ac.kr

†Present address: Department of Earth and Environmental Sciences, Korea University, Seoul 02841, Korea.

Published by the American Physical Society under the terms of the [Creative Commons Attribution 4.0 International license](https://creativecommons.org/licenses/by/4.0/). Further distribution of this work must maintain attribution to the author(s) and the published article's title, journal citation, and DOI.

FeO₂ [16]). There are two structures with the space group $Pa\bar{3}$: the pyrite-type (FeS₂) and the high-pressure PdF₂-type (HP-PdF₂). They can be distinguished by whether there is anion-anion bonding (pyrite) or not (HP-PdF₂). The $Pa\bar{3}$ -type oxides are commonly referred to as the pyrite type [3,12]; however, based on bond distances, GeO₂ and SiO₂ are not expected to have O-O interactions [12,17,18]. Thus, it is more appropriate to refer to the high-pressure $Pa\bar{3}$ -type oxides as the HP-PdF₂-type structure.

In the HP-PdF₂-type structure the cations are arranged in a distorted corner-sharing octahedral environment (see Fig. S1 of Supplemental Material [19]). The HP-PdF₂-type and post-HP-PdF₂ phases have yet to be identified under dynamic compression in any oxide materials. Theoretical calculations predict transformation to post-HP-PdF₂-type phases in GeO₂ including the orthorhombic cotunnite-type ($Pnam$) at ~ 300 GPa and the hexagonal Fe₂P-type ($P\bar{6}2m$) structure at ~ 600 GPa [18]. In the cotunnite-type structure, the CN of the Ge cation is 9 and the oxygen ions adopt a distorted hexagonally close-packed arrangement generating tricapped trigonal prisms sharing an edge along the a axis and parallel to the c axis. In the Fe₂P-type structure, the Ge cations are also coordinated to 9 oxygens forming tricapped trigonal prisms which are connected to each other by edge sharing along the a direction and by face sharing along the c direction (Fig. S1 [19]).

The behavior of amorphous GeO₂ has been extensively studied at high pressures as a model system for understanding coordination changes and amorphous structures in a low-pressure analog for silicate glass [20–25]. Above 90 GPa, the CN of GeO₂ glass is reported in one study to be greater than 7, which exceeds that of the HP-PdF₂-type structure [23]. Other work has reported a HP-PdF₂-like structure and compressibility of the glass above 100 GPa [24,25]. A detailed understanding of crystalline GeO₂ phases is useful in interpreting observations of amorphous counterparts at very high pressure [24,26,27].

Ramp compression is a dynamic-loading technique that can compress materials to the terapascal pressure range within the solid state, far in excess of pressures attainable in conventional static compression experiments [28]. Ramp loading is analogous to compressing a material by a series of weak shocks, thereby greatly reducing the heating arising from the increased entropy associated with single-shock compression. Ramp compression, in combination with *in situ* x-ray diffraction (XRD), allows for the observation of the atomic-level structure of materials up to ~ 2 TPa [28–35]. Studies of the atomic-level structures of high-pressure phases formed under dynamic compression at hundreds of GPa pressures have so far mostly been restricted to high-symmetry phases and simple phase transitions such as the fcc-hcp-bcc phases of elemental metals (Al, Fe, Au, Mo, Sn, etc.) [29–32,36,37] or B3-B1-B2 phases of binary compounds (MgO, FeO, and SiC) [33–35]. More generally, the atomic-level structure

achieved in oxides and silicates under dynamic loading (both shock and ramp) to Mbar pressures and beyond is poorly constrained [38–40]. Phase transitions are observed to occur under shock loading for many minerals, but the *in situ* atomic structure of the high-pressure phases are largely unknown [40].

In this study, GeO₂ is examined by x-ray diffraction under ramp compression to nearly 900 GPa, more than 5 times the pressures reached in previous static and shock compression studies on this material. Our diffraction data provide experimental evidence for the persistence of the HP-PdF₂-type structure up to 440 GPa followed by a phase transition to a post-HP-PdF₂-type phase consistent with the cotunnite-type structure.

II. MATERIALS AND METHODS

A. Target assembly and laser-driven compression

Polycrystalline α -quartz-type GeO₂ (Aldrich, >99.998% purity) is ground until the grain size is reduced to a few microns. The phase and purity of the sample are confirmed by Raman spectroscopy and x-ray diffraction [11]. The sample powder is compressed to 3 GPa in a diamond-anvil cell producing 10–19- μ m-thick pellets. This resulted in low-porosity ($\sim 3.6\%$) aggregates as estimated from scanning electron microscopy images [41] (see Supplemental Material Fig. S2 [19]). The sample pellet is glued between a diamond ablator and a LiF window for low-stress experiments (< 400 GPa) [Fig. 1(a)] or between two diamonds for high-stress experiments (> 400 GPa) [inset of Fig. 2(a)]. The high-stress targets also contain a thin Au layer (~ 1 μ m thick) which acts as a shield to prevent heating by x rays emitted from the drive plasma. All layers are attached with ~ 1 - μ m-thick epoxy layers. Ta, W, or Fe foils (75–150 μ m thick) with a 300- μ m-diameter aperture are attached to the back of the target package [see Fig. 1(a) and Table S1 of the Supplemental Material [19]]. These are used for x-ray collimation and to provide reference diffraction lines for calibrating the x-ray diffraction geometry.

LiF has been previously reported to remain transparent when compressed to at least 800 GPa under ramp loading [42], but loses transparency at ~ 400 GPa under laser-driven shock compression [42]. In our ramp experiments, LiF is observed to become opaque above ~ 400 –450 GPa. This can be explained by steepening of the ramp into a shock wave after it enters into the LiF window. For this reason, the use of LiF windows is restricted to lower-stress conditions.

Ramp-compression experiments are performed using the Omega-60 and Omega-EP laser facilities at the Laboratory for Laser Energetics at the University of Rochester. At Omega-60, 3–6 laser pulses (1–3.7 ns in duration) are staggered in time to produce a composite ramp-shaped pulse (see Fig. S5 in Supplemental Material [19]). At Omega-EP, a single beam is used to create a 10-ns duration pulse

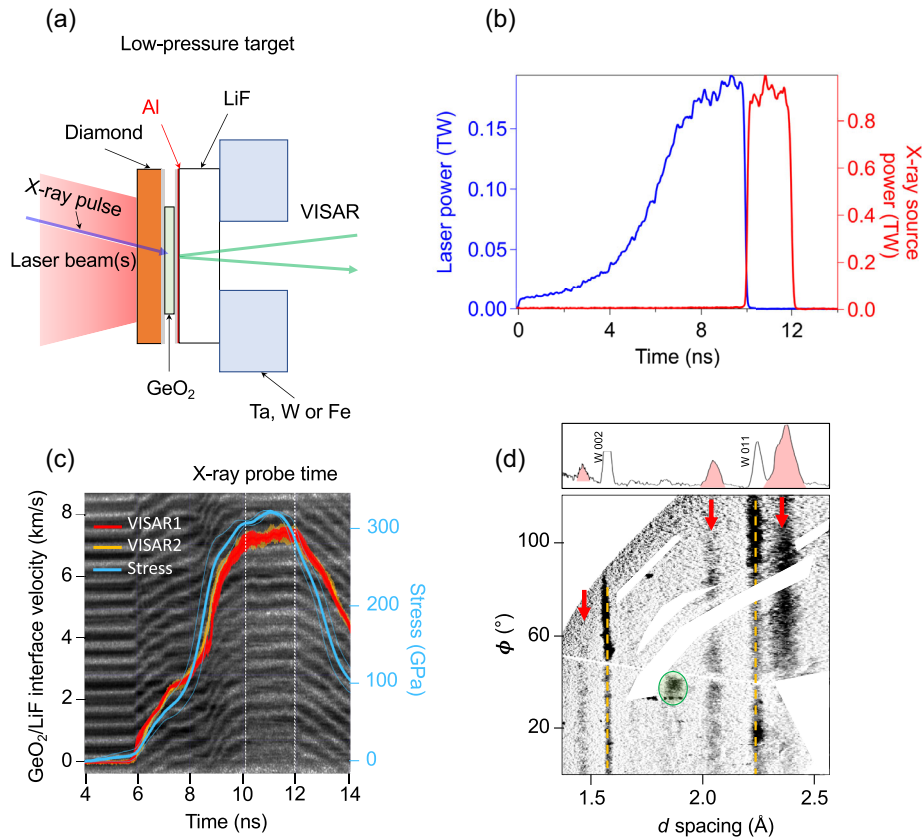


FIG. 1. Experimental setup and representative results from laser-driven ramp compression combined with x-ray diffraction. (a) Schematic target assembly for low-stress experiments consisting of a diamond ablator, GeO_2 sample, and Al-coated LiF window attached to a metal foil with an aperture. (b) Drive laser pulse for shot no. 34587 (blue trace). X rays are generated using a 2 ns square pulse (red trace). (c) The extracted interface velocity history for shot no. 34587 from each of two VISARs (red and orange traces) is used to determine sample stress (blue trace) during the x-ray probe period (gray dotted lines). The stress in this experiment is 321(13) GPa. (d) Projection of representative image plate data into d -spacing ϕ coordinates, where ϕ is the azimuthal angle around the incident x-ray beam. The yellow vertical dashed lines indicate diffraction peaks from the uncompressed tungsten foil used for calibrating the image plates. The green ellipse shows single-crystal Laue diffraction from LiF which can be identified as highly textured, localized peaks in contrast to the extended lines of GeO_2 . The red arrows indicate the diffraction peaks from the HP-PdF₂-type structure of GeO_2 . An integrated one-dimensional diffraction pattern is shown at the top.

[Fig. 1(b)]. Distributed phase plates are used to produce an 800- or 1100- μm focal spot with a super-Gaussian profile. The peak laser drive irradiance in these experiments ranges from 1.1×10^{13} to 6.6×10^{13} W/cm^2 . The ramped shapes are tuned to avoid strong shock formation in the sample. The laser pulses generate ablation-pressure compression waves which propagate through the target assembly. Multiple wave reverberations at the sample layer boundaries contribute to produce uniform high-stress conditions in the sample for about 1–2 ns near peak compression (see Fig. 2 herein and Fig. S5 in Supplemental Material [19]).

B. *In situ* x-ray diffraction measurements

A 1–2-ns pulse of quasimonochromatic helium- α (He_α) x rays is generated by irradiating foils of Fe ($\text{He}_\alpha = 6.683$ keV), Cu ($\text{He}_\alpha = 8.368$ keV), Zn ($\text{He}_\alpha = 8.975$ keV), or Ge ($\text{He}_\alpha = 10.249$ keV) using 16–18 beams with energies of 400–500 J/beam at Omega-60 or 1–3 beams with energies

of 1250–1950 J/beam at Omega-EP [43]. The foils are positioned 17–24 mm from the target and at 22.5° (Omega-EP) or 45° (Omega-60) from the target normal. The laser pulses are timed to generate x rays for probing the sample at predicted peak stress conditions. Diffracted x rays are recorded on image plate detectors positioned behind the sample. Metal filters (12.5- μm -thick Fe, Cu or 50–100- μm -thick Al) are used to attenuate higher energy lines including H_α , He_β , and He_γ x rays, and the bremsstrahlung x-ray background from the drive plasma [43]. The XRD pattern recorded onto the image plates are projected into 2θ - ϕ space (2θ is the scattering angle and ϕ is the azimuthal angle around the incident x-ray beam). A sensitive nonlinear iterative peaks (SNIP) algorithm [44] is used to subtract the background. Interplanar d spacings are determined from the measured diffraction angles using Bragg’s law: $\lambda = 2d \sin(\theta)$, where λ is the x-ray wavelength. All image plates and the integrated diffraction patterns are shown in Fig. S3 [19]. The uncertainty in the d spacings includes the following sources: (1) variation

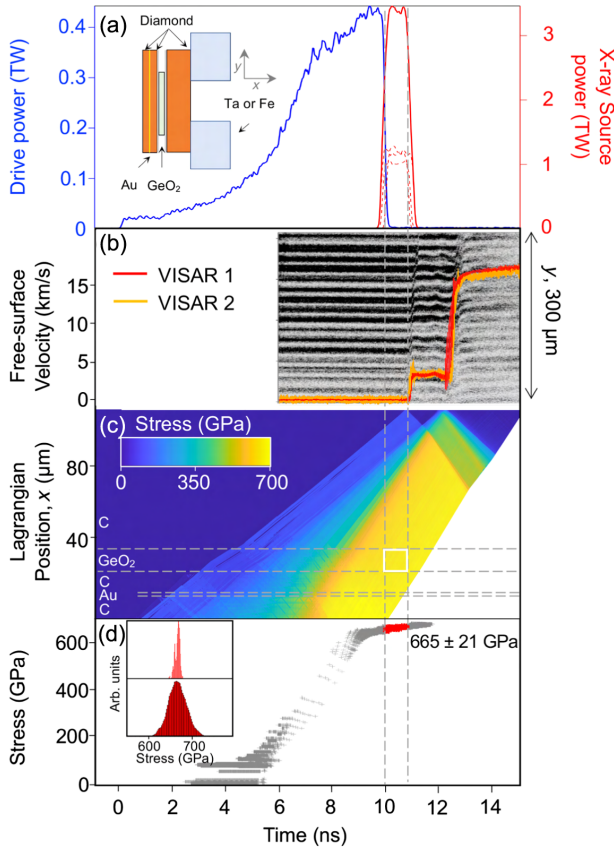


FIG. 2. Timing and stress determination for a representative GeO_2 ramp-compression experiment (shot no. 34583) using a diamond window. (a) Drive laser pulse shape (blue). X rays are generated using 1 ns square pulses (red trace). The inset shows the target assembly for high-stress experiments (>400 GPa). (b) Interferogram from the VISAR records diamond free-surface velocity (red and orange curves) that is used to determine the stress history within the sample. (c) Calculated stress distribution within the target assembly as a function of time determined by the backward characteristics analysis (see Sec. II D). The horizontal dashed lines represent the material layers in Lagrangian coordinates. (d) Calculated stress history of the GeO_2 sample as a function of time. The vertical dashed lines represent stress states over the x-ray probe period. The inset shows the histogram of GeO_2 stress states (upper) and that of the Monte Carlo analysis (lower).

in the measured value of 2θ as a function of azimuthal angle (ϕ), (2) uncertainty in fitting the sample peak positions to Gaussian profiles, (3) the uncertainty in the measured thickness of each layer in the target package, and (4) the uncertainty in the incident x-ray wavelength (<0.01 Å) [43]. Diffraction lines from the sample are compared to expected peak positions for candidate structures, allowing them to be indexed. The unit cell volume and density of GeO_2 are obtained using weighted least-squares fitting from the observed d spacings. The resultant d spacings and densities and their uncertainties for the best fitting structures are given in Supplemental Material Tables S2 and S3 [19].

C. Optimized x-ray sources for x-ray diffraction at the Omega laser facility

In order to enhance the x-ray intensity of the low-symmetry structure, we implement modifications to the conventional experimental configuration. These modifications include (1) the relocation of the x-ray source to a position closer to the sample, from 24.14 to 17 mm, which results in a twofold increase in x-ray flux; (2) an improvement in sample preparation techniques to enable the fabrication of dense, low-porosity samples by a diamond-anvil cell; and (3) the use of thick samples, with a thickness of up to approximately $20 \mu\text{m}$, in order to maximize diffraction intensity while avoiding the formation of shock waves within the sample and maintaining maximum uniform stress. If the sample is excessively thick, the ramp wave steepens to form a shock which could result in sample melting or difficulty in determining the compression history of the sample.

Furthermore, we have made continuous improvements in recent years to enhance the ability to record diffraction from low- Z , low-symmetry materials at high stress. These improvements involve optimizing x-ray source foils and geometric parameters, improving filtering, and using effective combinations of x-ray sources and pinhole material [43]. In particular, the development of a higher energy Ge He_α source provides greater spectral decoupling from the drive plasma x ray, allowing the use of thicker filters in front of image plates and improving the results of higher-stress shots (above ~ 500 GPa). We have also developed the analysis code for the velocity interferometer system for any reflector (VISAR) and diffraction that can correct systematic errors to pinhole and sample 2θ , improve the nonlinear background subtraction algorithm, and better identify and locate the positions of sample and pinhole diffraction lines [44,45].

D. Stress determination

The velocity at the interface between the sample and the LiF window (for low-stress shots, <400 GPa) or the free-surface velocity of the rear diamond (for high-stress shots, >400 GPa) is measured using a line-imaging VISAR [46] to determine the stress history within the sample [Figs. 1(b) and 2]. The VISAR, using a 532-nm laser, monitors the Doppler shifts reflected from the accelerating surface as a function of time through a rear aperture in the target assembly. Two VISAR channels with different velocity sensitivities (see Table S1 in Supplemental Material [19]) are used to remove velocity ambiguities in the fringe signal. Example velocity profiles and their calculated stress histories are shown in Figs. 1(c), 2(b), and 2(d).

For targets with a LIF window, the VISAR records an apparent GeO_2 -LiF interface particle velocity which is corrected for the stress-induced change in refractive index of LiF to obtain the true interface particle velocity [47,48] [Fig. 1(c)]. The stress history within the sample is

determined assuming that ramp loading can be approximated as an isentropic compression pathway and, as such, that the thermodynamic parameters propagate at the local sound speed. The stress conditions are calculated by solving a grid of forward- and backward-propagating characteristics with the boundary conditions at the sample-LiF interface [49,50]. The tabular equations of state (EOS) required for this analysis were taken either from the SESAME [51] or Livermore (LEOS) [49] libraries. We use SESAME no. 7271v3 for LiF and no. 7830 for diamond. There is no available EOS table for quartz-type GeO_2 . As a consequence, the LEOS table for Ti (no. 722) is chosen as a substitute as its pressure-particle velocity relationship is intermediate between those of rutile-type and GeO_2 glass (see Fig. S4 [19]). Note that the stress conditions calculated within the sample are largely insensitive to the sample EOS after several reverberations between the boundary of layers of the sample. For targets with a diamond window, the free-surface velocity [Fig. 2(b)] is used as a boundary condition for a backward characteristics analysis to calculate stress using the previously measured pressure-density-particle velocity relationships for diamond [49,50,52,53]. No correction has been made between the longitudinal stress and the corresponding hydrostatic pressure as the strength of GeO_2 under these conditions is unknown.

The uncertainties in the stress are determined using a Monte Carlo (MC) routine that performs 1000 characteristics calculations for each shot. The MC simulation includes the following uncertainties: (1) uncertainty in the measured thickness of each layer in the target package ($\sim 1 \mu\text{m}$); (2) uncertainty in the particle velocities (u_p) and Lagrangian sound speed (C_L) calculated from the equations of state for LiF, Ti, and diamond (2%); (3) uncertainty in the velocity determination VISAR (5% of the velocity-per-fringe constant); and (4) uncertainty in the timing of the x-ray probe (60 ps uncertainty) [30]. For stresses above 800 GPa, the uncertainty in the diamond EOS is increased to 5% to reflect greater uncertainty as the measured diamond ramp-compression data extend only up to 800 GPa [52]. Each MC iteration propagates these inputs through forward- and backward- or backward-propagating characteristics (depending on whether a LiF or diamond window is used) and extracts the pressure distribution within the sample during the x-ray probe time. The stress distribution is fit to a Gaussian distribution and its uncertainty is determined from the standard deviation of the fit. Shots with multimodal stress distributions may occur due to imperfectly predicted optimum x-ray probe time. If the x-ray probe pulse is slightly mistimed during peak pressure, the sample may experience regions with different stresses due to the ramp loading process. In such a case, the total stress distribution is fit to a small number of Gaussians.

A systematic correction needs to be applied to targets with diamond windows as the strength of diamond upon

unloading is unknown. There are two end-member cases: either the diamond retains its strength upon unloading or it undergoes a strength collapse and has no strength upon unloading. In our analysis, we assume that the diamond's strength is maintained during both compression and release along the reversible isentropic path. This assumption may result in a systematic underestimation of the final stress if strength collapse occurs [32]. Hydrodynamic simulations show a difference in the sample stresses between two cases up to 50 GPa. As a result, an additional positive 50 GPa is added in quadrature to the stress uncertainty for samples with diamond windows resulting in an asymmetric error bar. The laser power, stress history, and velocity profiles for all shots are shown in Fig. S5 of the Supplemental Material [19].

III. RESULTS

Sixteen shots are performed on GeO_2 covering the stress range 154(19)–882(28) GPa. Representative x-ray diffraction data are shown in Fig. 3 and the full set of diffraction

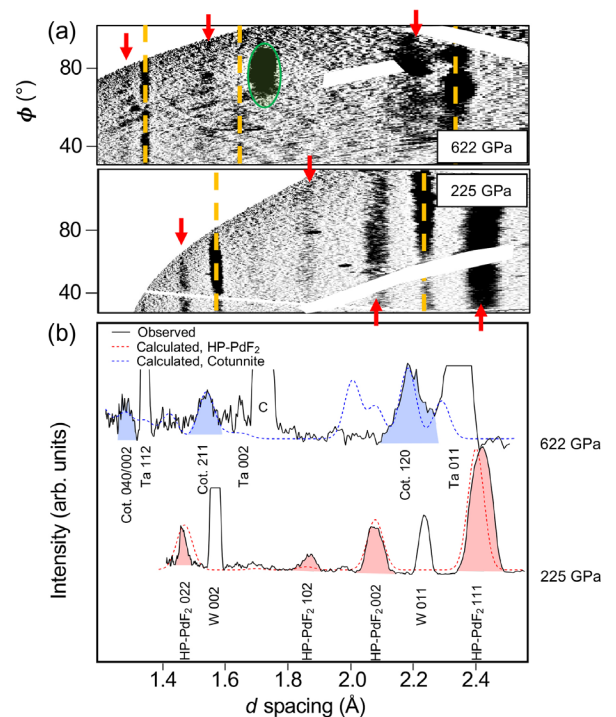


FIG. 3. Representative XRD images (upper) and integrated one-dimensional diffraction patterns (lower) for ramp-compressed GeO_2 . (a) The red arrows indicate the diffraction peaks from the sample. The green ellipse shows single-crystal Bragg diffraction from diamond, which can be identified as highly textured, localized peaks compared to the extended lines of GeO_2 . Yellow dashed lines denote diffraction from the Ta or W pinhole substrate. Pink and blue shaded peaks show the observed GeO_2 diffraction lines compared with the calculated diffraction pattern for the HP-PdF₂-type structure at 225 GPa (red dashed line) and cotunnite-type structure at 622 GPa (blue dashed line), respectively. “C” denotes a single-crystal spot corresponding to the green ellipse.

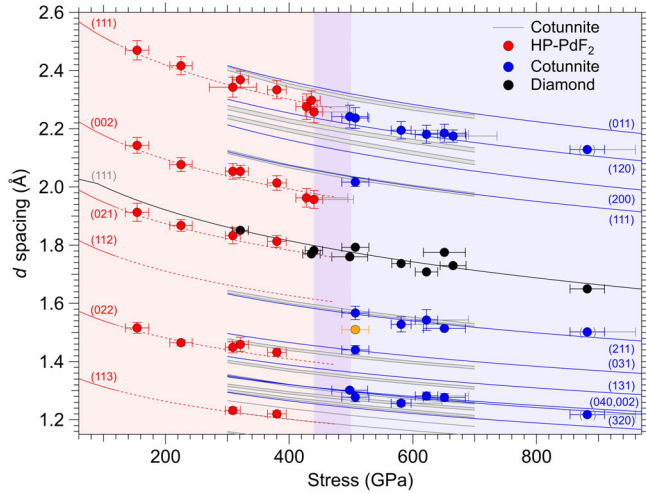


FIG. 4. Measured d spacings as a function of stress for GeO_2 . The red and blue circles represent the observed diffraction peaks assigned to HP-PdF₂ structure from 154(19) to 440(−17, +52) GPa or to the cotunnite-type structure above 498(29) GPa. The red lines are predicted d spacings from the HP-PdF₂-type structures based on extrapolations of lower-pressure experimental data [11]. The blue lines are calculated d spacings from the cotunnite-type structure based on our work (see Fig. 6) compared with those from *ab initio* calculations (gray bands) [18]. The purple shaded region shows the range of the possible transition region. The d spacing for the diamond (111) peak, calculated from the ramp equation of state [52] and extrapolated to pressure higher than 800 GPa, is shown as the black curve. Gray error bars represent an additional positive stress uncertainty GeO_2 due to uncertainty in the strength of diamond. An unindexed peak at 507 GPa is shown as yellow.

images are contained in the Supplemental Material (Fig. S3 [19]). At stresses up to 440(−14, +52) GPa, 1–5 sample diffraction lines are observed and these define consistent trends in d spacing as a function of stress (Fig. 4). As the cubic $Pa\bar{3}$ -type phase (HP-PdF₂-type) is observed in static experiments to 120 GPa [11] and theoretically predicted to remain stable above 200 GPa [18], we first attempt to index our observed data to this structure. Figure 4 compares the expected d spacings for the HP-PdF₂-type phase (red lines) determined from 300 K static EOS data [11] and extrapolated at pressures above 120 GPa (dashed lines). The observed diffraction lines from 154 to 440 GPa are consistent with the expected positions for the HP-PdF₂-type structure. For the shot at 372(16) GPa, as many as five sample diffraction lines corresponding to the (111), (002), (021), (022), and (113) reflections of the HP-PdF₂-type structure are observed allowing for redundant constraints on the lattice parameter and density of this cubic phase (see Fig. 4 herein and Table S2 of the Supplemental Material [19]). Figure 5 compares the density of GeO_2 in the HP-PdF₂-type phase with extrapolations of previous 300 K static data (red dashed lines) for this structure [11,18] showing good overall agreement.

At 498(29) GPa, only two diffraction peaks are observed as the reflections assigned to (021) and (022) at lower stresses are not detected. One of two observed peak is at around ~ 1.3 Å, which cannot be indexed using the HP-PdF₂ structure. The (002) peak of the HP-PdF₂-type phase is not apparent above 440 GPa, and the stress dependence of the d spacing of (111) peak undergoes a subtle shift to lower d spacings. Taken together, this is a clear indication of a change in the diffraction patterns at 498 GPa and above, indicating a structural transition. At 428–440 GPa where only 1–2 diffraction peaks are observed at each stress, a mixed-phase region may exist. In experiments above 498 GPa, three diffraction peaks are consistently observed up to the highest stress, 882(28) GPa. These three lines follow a consistent trend of d spacings under compression (Fig. 4).

To investigate possible structures, we examine candidate post-HP-PdF₂ phases such as the $R\bar{3}$ phase [8] and the Fe₂P-type phase [18], but the densities calculated from assigning the observed diffraction peaks to these phases are much less than the expected density range of the Fe₂P-type structure (Fig. S6 in Supplemental Material [19]). Furthermore, the calculated densities of these are generally smaller than the expected density of the HP-PdF₂-type structure. These phases can thus be ruled out as a high-pressure phase transition should not result in a volume increase.

We also consider the cotunnite-type phase as a candidate structure as this is predicted to be the thermodynamically stable phase of GeO_2 above 300 GPa [18]. Two of the observed peaks can be indexed as (120) and (211) reflections of the cotunnite-type phase, which are expected to be high-intensity reflections of the cotunnite-type phase in other dioxides [14,15,54]. The other peak occurs at d spacings near those expected for the nearly overlapping (002) and (040) reflections which are predicted to be moderate-intensity reflections (Fig. 4).

Three peaks are the minimum number required to constrain the lattice parameters of an orthorhombic structure. In this case, we use the (120), (211), and combined (002) and (040) to obtain cotunnite lattice parameters (Fig. 6), with one observed peak assigned simultaneously to the (002) and (040) reflections. Alternative fits where the third peak is assigned to either the (002) or (040) reflection of the cotunnite-type phase are shown in Fig. S7 [19].

The three reflections are consistently observed for GeO_2 between 507(22) and 882(28) GPa (Fig. 4), suggesting the high-pressure phase persists over this region. The lattice parameters of the cotunnite-type unit cell determined from our data are compared with those predicted by computer simulations [18] in Fig. 6. For one shot at 507(22) GPa, five diffraction peaks are observed and assigned to the (120), (111), (211), (031), and (040)/(002) reflections of the cotunnite-type structure (Fig. 4 herein and Fig. S3 in Supplemental Material [19]). An additional weak peak observed at 1.51(1) Å cannot be explained by the

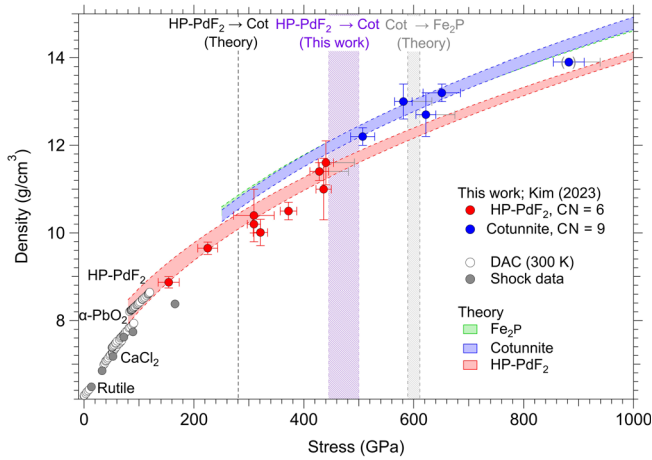


FIG. 5. Density of GeO_2 as a function of stress. The density of ramp-compressed GeO_2 is determined assuming an HP-PdF_2 -type (red) and cotunnite-type structure (blue). These are compared with the range of densities obtained from first principles calculations [HP-PdF_2 [11] (red), cotunnite [18] (blue), and Fe_2P [18] (green) shaded regions, the latter of which nearly overlaps the cotunnite region]. Open symbols are static diamond-anvil cell (DAC) data [11]. Previous shock compression data [20] (gray circles) are also plotted. The stress ranges of the phase transformation from the HP-PdF_2 -type structure to the cotunnite-type structure from theory [18] and this work, and further transition to Fe_2P -type structure [18] from theory, are shown as the black dashed line, purple shaded region, and gray shaded region, respectively. Gray error bars represent an additional positive stress uncertainty GeO_2 due to uncertainty in the strength of diamond.

cotunnite-type structure (Fig. S3 [19]). This peak is not detected at any other pressures.

The observed diffraction peaks are generally consistent with the predicted cotunnite-type structure (gray band) from *ab initio* density functional theory (DFT) although our observed d spacing for (120) deviates from the calculated values from DFT (Fig. 4). This possibly indicates the effect of deviatoric stress on the lattice parameters of the anisotropic cotunnite-type structure at high stress, or uncertainty in the theoretical calculations. The d spacings of the cotunnite phase (blue lines in Fig. 4) are calculated by fitting our ramp-compression data to a linearized Birch-Murnaghan equation [55] which is used here as a convenient fitting curve. The axial moduli are fixed at values obtained from numerical simulations at 0 K using the local density approximation of DFT at pressures between 300 and 700 GPa [18] (see Fig. 6 herein and Table S4 of the Supplemental Material [19]). The calculated d spacings and intensities of the cotunnite-type GeO_2 at 600 GPa inferred from our experimental data are listed in Table S5 of the Supplemental Material [19]. The lattice parameters obtained from our data are compared with those predicted by theory [18] in Fig. 6. Nonhydrostatic stress under dynamic loading may affect the lattice parameters as

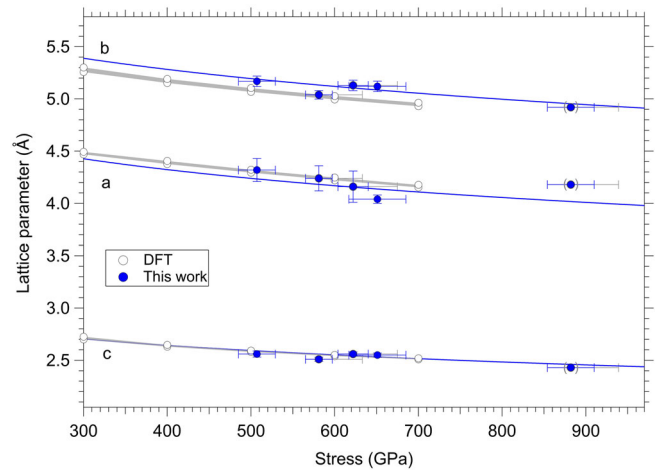


FIG. 6. Lattice parameters of cotunnite-type GeO_2 as a function of stress (blue symbols). The open symbols are from density functional theory calculations (DFT) at 0 K [18]. The lattice parameters are constrained from the observed diffraction lines which are assigned to (120), (211), and (002) and (040) reflections of the cotunnite-type structure of GeO_2 . The lattice parameters assuming the peak is assigned to either (020) and (004) reflection of the cotunnite-type structure of GeO_2 are shown in Figure S7 of Supplemental Material [19]. The blue curves are from fitting our ramp-compressed data to a linearized Birch-Murnaghan equation [55]. Gray error bars represent an additional positive stress uncertainty GeO_2 due to uncertainty in the strength of diamond.

observed in other studies [40,56,57]. The corresponding densities (shown as blue symbols) are larger than those of the HP-PdF_2 -type phase and are generally consistent with DFT at 0 K (Fig. 5) [18].

As an additional test of our peak assignment, we compare the GeO_2 diffraction data to an experiment conducted on tin dioxide SnO_2 at 137(13) GPa under ramp loading using a nearly identical experimental procedure (Fig. S8 [19]). GeO_2 and SnO_2 are both group 14 dioxides, and expected to have similar phase transitions, but occurring at lower pressures in SnO_2 due to its larger ionic radius. The cotunnite-type phase of SnO_2 has been experimentally observed over the range from 54 to 203 GPa at high temperature [14,54] and is theoretically predicted to be stable up to 600 GPa [54]. Thus, cotunnite is the expected phase at 137 GPa. As shown in Fig. S8 [19], we observe three diffraction lines from SnO_2 at this stress which have similar relative positions to the three peaks observed in our GeO_2 data above 498 GPa, suggesting the two materials are adopting the same structure. The three peaks from SnO_2 can also be indexed to the (120), (211), and (004)/(020) reflections from the cotunnite-type structure as found for GeO_2 . The calculated density for this experiment on ramp-compressed SnO_2 is 11.4(5) g/cm^3 which is within $\sim 0.2\%$ of that predicted from previous

studies [14,54]. Thus, the diffraction data for SnO_2 are consistent with the expected cotunnite structure for this material, and the similarity of the diffraction data suggests that GeO_2 adopts the same phase. This supports our conclusion that the diffraction data for the post-HP-PdF₂ phase of GeO_2 are most consistent with the cotunnite-type structure.

It should be noted that the (111) reflection of cotunnite-type GeO_2 , which is expected to have strong intensity (Table S5 [19]), is not observed in our experiments except the shot at 507(22) GPa. The reason for the differences in this shot compared to others above 498 GPa is unknown. This reflection is also absent in ramp-compressed SnO_2 at 137 GPa (Fig. S8 [19]). The failure to detect this peak in these materials might be a consequence of texture development under nonhydrostatic loading on the nanosecond timescales of ramp-compression experiments. The intensity of the (111) reflection of the cotunnite-type phase has been observed to be relatively weaker than expected in other oxides in static compression experiments in which transformation to the cotunnite-type structures occurs under room-temperature compression [58,59].

The higher laser-drive energies used to achieve higher *in situ* stresses increases the ablation background resulting in a diminished signal-to-noise ratio for the diffraction pattern, which may prevent the observation of more than a few high-intensity diffraction peaks. The limited number of observed diffraction peaks makes it difficult to unambiguously identify lower-symmetry phases under laser-driven ramp compression. Despite this limitation, the cotunnite-type structure best matches the observed diffraction peaks in terms of d spacings, lattice parameters, and densities. Furthermore, the temperature under ramp loading lies between the principal Hugoniot and isentrope, indicating that ramp-compressed materials can be less dense than predicted using first principle calculation at 0 K. An estimate of lower-bound temperatures achieved in our experiments is shown in Fig. 7.

In the highest stress shot at 882 GPa, the diffraction peaks from the Ta pinhole material are not observed (Figs. S3 and S9 [19]). This is likely because the absorption edge of Ta ($L_3 = 9.881$ keV) is just below the He_α energy (10.249 keV) of Ge resulting in preferential absorption of the incident radiation. The 2θ values could still be estimated by using the geometric calibration parameters from the previous shot which used the same experimental configuration. The accuracy of the transferred calibration, however, is limited due to small positional variation of the placement of the x-ray source and the image plates. Hence, while the data from this shot are only semiquantitative, they are consistent with the trend of the lower-pressure data. Three diffraction lines are again observed at this pressure that can be assigned to the (120), (211), and (040)/(002) reflections of cotunnite. The d spacings of the observed peaks are consistent with extrapolation of lower-pressure

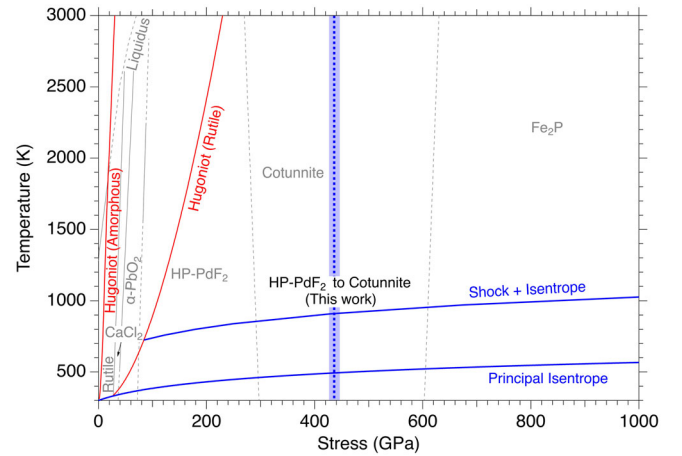


FIG. 7. Phase diagram of GeO_2 with phase boundaries [60–62], estimated Hugoniot of amorphous [63] and rutile-type GeO_2 , and predicted thermodynamic paths. The theoretical Hugoniot (rutile) is calculated from the thermodynamic parameters listed in Table S6 of Supplemental Material [19]. The blue curves indicate the stress and temperature paths along the principal isentrope and an initial shock (~ 84 GPa) followed by isentropic compression as a lower bound in this work. The blue dashed line indicates the estimated stress for the phase boundary between HP-PdF₂ phase to cotunnite-type phase of GeO_2 from this work. Because of the unknown strength of GeO_2 , the temperature conditions under ramp loading are uncertain and the shock + isentrope curve serves as a lower bound.

data. However, the diffraction data for this shot only provide a guide for phase identification but do indicate that the phase observed above 498 GPa remains stable to as high as 882 GPa.

IV. DISCUSSION

Because of the ability to achieve extreme compression without melting, laser-based ramp compression has opened new opportunities to use pulsed x-ray diffraction to examine crystal structures formed at extreme conditions, far beyond the limits of conventional static compression experiments [64]. To date, only a few studies have been performed on geological materials that are relevant to rocky exoplanetary mantles. Transformation to the B2 CsCl-type phase has been observed at multihundred GPa pressures in MgO and FeO [33,34]. SiC adopts the B1 NaCl structure over the range from 0.14 to 1.507 TPa [35]. Diamond was not observed to undergo any phase transitions up to 2 TPa [28].

A recent study of laser-shocked polycrystalline stishovite revealed no phase transformations and remarkable persistence of the rutile-type structure to 336 GPa, well beyond its expected stability limit of ~ 60 GPa [56]. Furthermore, shock-compression studies on silicates with *in situ* x-ray diffraction have observed transformation to

amorphous, not crystalline, phases above 80 GPa [38,40]. Shock melting occurs below 200 GPa for many oxides and silicates. Thus, shock compression is restricted in its ability to synthesize and characterize high-pressure crystalline phases of silicates at extreme conditions (>100 GPa). Our work shows the advantages of ramp compression to constrain the phase transitions and atomic-level structures of geological materials from multihundreds of GPa through TPa pressures [35].

Previous dynamic compression data on GeO₂ are limited to shock experiments on rutile-type and amorphous GeO₂ up to 160 GPa with evidence for a high-pressure phase transition at 70–90 GPa [20]. GeO₂ glass has been the subject of extensive static high-pressure studies reaching up to 133 GPa with conflicting evidence reported for development of coordination numbers greater than six [23–25]. At higher pressures, theoretical studies predict crystalline transformations in GeO₂ to a cotunnite-type structure at ~300 GPa and to an Fe₂P-type structure at 600 GPa [18].

Our study shows that under ramp compression of the α -quartz-type GeO₂, the HP-PdF₂-type structure can be synthesized and persists up to 440 GPa, well above the theoretically predicted transformation pressure. This indicates that the HP-PdF₂-type structure of GeO₂ may be a metastable phase above 300 GPa, or that theoretical studies need to be reevaluated. Recent studies on ramp-compressed silicon also reveal that higher pressure than predicted by theory is required for a phase transition [65]. This shows that ramp compression can be used to synthesize theoretically predicted stable high-pressure phases in dioxides, although overpressurization may be needed relative to thermodynamic equilibrium phase boundaries.

We further observe evidence for a post-HP-PdF₂-type phase between 498 and 882 GPa. Our diffraction data are best explained by the formation of the cotunnite-type structure. Our results thus show that laser-based ramp compression can produce new phases with very large cation coordination increases from 4 (the α -quartz-type phase starting material) to 9 (the cotunnite-type phase).

Identifying low-symmetry phases is challenging when using pulsed x-ray diffraction at extreme pressures. The strong x-ray background produced by the drive plasma combined with the limited fluence of laser-based x-ray sources and the short integration time make it very challenging to observe more than a few peaks. This is especially true for low atomic number materials such as silicates. In this study, we are able to consistently detect three or more diffraction peaks across a range of stress conditions up to the peak pressure. The diffraction data are consistent with the orthorhombic cotunnite-type phase and inconsistent with other possible high-pressure phases (of rhombohedral or hexagonal symmetry). This demonstrates that the detection of low-symmetry phases in low-*Z* compounds is feasible. As x-ray diffraction techniques

under ramp compression advance and new facilities (e.g., the NIF, Laser Megajoule) develop, the capabilities for these kinds of studies will only improve and will likely allow studies on lower-*Z* materials such as SiO₂ and other silicates.

V. CONCLUSIONS

The ultrahigh-pressure phases of SiO₂ are important for understanding the dynamics of the lower mantles and at the core-mantle boundaries of large rocky planets. GeO₂ is considered to be a useful analog material for SiO₂ [2]. Here we examine the crystal structure of GeO₂ under ramp loading with *in situ* x-ray diffraction. The GeO₂ α -quartz starting materials have transformed to the cubic HP-PdF₂-type ($Pa\bar{3}$) structure below 154 GPa. This is the phase of GeO₂ predicted to be thermodynamically stable from ~60 to 300 GPa, demonstrating that the lowest energy structure can be formed under ramp compression in GeO₂. We observe that the HP-PdF₂-type phase persists to 440 GPa, above its theoretically predicted upper stability limit (at 0 K). Above 498 GPa, a post-HP-PdF₂ phase is observed and assigned to the cotunnite-type phase ($Pnam$) based on its density and by comparison with ramp-compressed SnO₂. The cotunnite-type phase persists up to 882 GPa. This is consistent with theoretical predictions of the stability of this phase to at least 600 GPa. The structures in this work span a wide range of cation coordination values starting from 4 (α -quartz-type GeO₂) and reaching 6 or 6 + 2 (HP-PdF₂-type) and 9 (cotunnite-type), demonstrating that formation of highly coordinated crystalline phases is feasible from low-coordination starting materials under ~10-ns ramp compression. Our work also shows that low-symmetry structures can be identified under ramp compression, which is useful in probing geological materials, many of which are expected to have lower-symmetry, noncubic structures under the conditions of deep exoplanetary interiors.

ACKNOWLEDGMENTS

We thank Carol Davis (LLNL) and the staff of the Laboratory for Laser Energetics for their expert experimental assistance. This research was supported by the National Science Foundation (NSF) under EAR-1644614 and PHY-2020249 and NSF-MRSZECZ program (DRM-2011750) and the U.S. Department of Energy (DOE) under DE-NA0003611. Additional support was provided by the Princeton Center for Complex Materials (PCCM). The National Laser Users' Facility at the University of Rochester's L. L. E. is supported by the U.S. DOE under Cooperative Agreement No. DE-NA0001944. The LLNL codes AnalyzeVISAR and AnalyzePXRDIIP were used in this project. Portions of this work were performed under the auspices of the U.S. DOE by LLNL under Contract No. DE-AC52-07NA27344.

- [1] J. M. Leger and J. Haines, *Crystal Chemistry of the AX₂ Compounds under Pressure*, *Eur. J. Solid State Inorg. Chem.* **34**, 785 (1997).
- [2] V. P. Prakapenka, G. Shen, L. S. Dubrovinsky, M. L. Rivers, and S. R. Sutton, *High Pressure Induced Phase Transformation of SiO₂ and GeO₂: Difference and Similarity*, *J. Phys. Chem. Solids* **65**, 1537 (2004).
- [3] Y. Kuwayama, *The Pyrite-Type High-Pressure Form of Silica*, *Science* **309**, 923 (2005).
- [4] T. Tsuchiya and J. Tsuchiya, *Prediction of a Hexagonal SiO₂ Phase Affecting Stabilities of MgSiO₃ and CaSiO₃ at Multimegabar Pressures*, *Proc. Natl. Acad. Sci. U.S.A.* **108**, 1252 (2011).
- [5] S. Wu, K. Umemoto, M. Ji, C.-Z. Wang, K.-M. Ho, and R. M. Wentzcovitch, *Identification of Post-Pyrite Phase Transitions in SiO₂ by a Genetic Algorithm*, *Phys. Rev. B* **83**, 184102 (2011).
- [6] A. R. Oganov, M. J. Gillan, and G. D. Price, *Structural Stability of Silica at High Pressures and Temperatures*, *Phys. Rev. B* **71**, 064104 (2005).
- [7] K. Umemoto, *Dissociation of MgSiO₃ in the Cores of Gas Giants and Terrestrial Exoplanets*, *Science* **311**, 983 (2006).
- [8] C. Liu, J. Shi, H. Gao, J. Wang, Y. Han, X. Lu, H.-T. Wang, D. Xing, and J. Sun, *Mixed Coordination Silica at Megabar Pressure*, *Phys. Rev. Lett.* **126**, 035701 (2021).
- [9] K. D. Putirka, C. Dorn, N. R. Hinkel, and C. T. Unterborn, *Compositional Diversity of Rocky Exoplanets*, *Elements* **17**, 235 (2021).
- [10] K. D. Putirka and S. Xu, *Polluted White Dwarfs Reveal Exotic Mantle Rock Types on Exoplanets in Our Solar Neighborhood*, *Nat. Commun.* **12**, 6168 (2021).
- [11] R. Dutta, C. E. White, E. Greenberg, V. B. Prakapenka, and T. S. Duffy, *Equation of State of the α -PbO₂ and Pa $\bar{3}$ Type Phases of GeO₂ to 120 GPa*, *Phys. Rev. B* **98**, 144106 (2018).
- [12] S. Ono, T. Tsuchiya, K. Hirose, and Y. Ohishi, *High-Pressure Form of Pyrite-Type Germanium Dioxide*, *Phys. Rev. B* **68**, 014103 (2003).
- [13] K. Shiraki, T. Tsuchiya, and S. Ono, *Structural Refinements of High-Pressure Phases in Germanium Dioxide*, *Acta Crystallogr. Sect. B* **59**, 701 (2003).
- [14] S. R. Shieh, A. Kubo, T. S. Duffy, V. B. Prakapenka, and G. Shen, *High-Pressure Phases in SnO₂ to 117 GPa*, *Phys. Rev. B* **73**, 014105 (2006).
- [15] B. Grocholski, S.-H. Shim, E. Cottrell, and V. B. Prakapenka, *Crystal Structure and Compressibility of Lead Dioxide up to 140 GPa*, *Am. Mineral.* **99**, 170 (2014).
- [16] Q. Hu, D. Y. Kim, W. Yang, L. Yang, Y. Meng, L. Zhang, and H.-K. Mao, *FeO₂ and FeOOH under Deep Lower-Mantle Conditions and Earth's Oxygen-Hydrogen Cycles*, *Nature (London)* **534**, 241 (2016).
- [17] Y. Kuwayama, K. Hirose, N. Sata, and Y. Ohishi, *Pressure-Induced Structural Evolution of Pyrite-Type SiO₂*, *Phys. Chem. Miner.* **38**, 591 (2011).
- [18] H. Dekura, T. Tsuchiya, and J. Tsuchiya, *First-Principles Prediction of Post-Pyrite Phase Transitions in Germanium Dioxide*, *Phys. Rev. B* **83**, 134114 (2011).
- [19] See Supplemental Material <http://link.aps.org/supplemental/10.1103/PhysRevX.13.031025> for additional details about the target packages, experimental parameters, and Hugoniot calculations, including supplemental figures, and tables.
- [20] I. Jackson and T. J. Ahrens, *Shock-Wave Compression of Vitreous and Rutile-Type GeO₂: A Comparative Study*, *Phys. Earth Planet. Inter.* **20**, 60 (1979).
- [21] C. Liu, T. J. Ahrens, and N. S. Brar, *Effect of Phase Change on Shock Wave Attenuation in GeO₂*, *J. Appl. Phys.* **91**, 9136 (2002).
- [22] M. Micoulaut, L. Cormier, and G. S. Henderson, *The Structure of Amorphous, Crystalline and Liquid GeO₂*, *J. Phys. Condens. Matter* **18**, R753 (2006).
- [23] Y. Kono, C. Kenney-Benson, D. Ikuta, Y. Shibasaki, Y. Wang, and G. Shen, *Ultra-high-Pressure Polyamorphism in GeO₂ Glass with Coordination Number >6*, *Proc. Natl. Acad. Sci. U.S.A.* **113**, 3436 (2016).
- [24] S. Petitgirard, G. Spiekermann, K. Glazyrin, J. Garrevoet, and M. Murakami, *Density of Amorphous GeO₂ to 133 GPa with Possible Pyritelike Structure and Stiffness at High Pressure*, *Phys. Rev. B* **100**, 214104 (2019).
- [25] G. Spiekermann *et al.*, *Persistent Octahedral Coordination in Amorphous GeO₂ up to 100 GPa by K β '' X-Ray Emission Spectroscopy*, *Phys. Rev. X* **9**, 011025 (2019).
- [26] V. V. Brazhkin, A. G. Lyapin, and K. Trachenko, *Atomistic Modeling of Multiple Amorphous-Amorphous Transitions in SiO₂ and GeO₂ Glasses at Megabar Pressures*, *Phys. Rev. B* **83**, 132103 (2011).
- [27] Y.-H. Kim, Y. S. Yi, H.-I. Kim, P. Chow, Y. Xiao, G. Shen, and S. K. Lee, *Pressure-Driven Changes in the Electronic Bonding Environment of GeO₂ Glass above Megabar Pressures*, *J. Am. Chem. Soc.* **144**, 10025 (2022).
- [28] A. Lazicki *et al.*, *Metastability of Diamond Ramp-Compressed to 2 Terapascals*, *Nature (London)* **589**, 532 (2021).
- [29] S. K. Han, R. F. Smith, D. Kim, J. K. Wicks, J. R. Rygg, A. Lazicki, J. H. Eggert, and T. S. Duffy, *Polymorphism of Gold under Laser-Based Ramp Compression to 690 GPa*, *Phys. Rev. B* **103**, 184109 (2021).
- [30] D. N. Polsin *et al.*, *X-Ray Diffraction of Ramp-Compressed Aluminum to 475 GPa*, *Phys. Plasmas* **25**, 082709 (2018).
- [31] J. Wang, F. Coppari, R. F. Smith, J. H. Eggert, A. E. Lazicki, D. E. Fratanduono, J. R. Rygg, T. R. Boehly, G. W. Collins, and T. S. Duffy, *X-Ray Diffraction of Molybdenum under Ramp Compression to 1 TPa*, *Phys. Rev. B* **94**, 104102 (2016).
- [32] J. K. Wicks, R. F. Smith, D. E. Fratanduono, F. Coppari, R. G. Kraus, M. G. Newman, J. R. Rygg, J. H. Eggert, and T. S. Duffy, *Crystal Structure and Equation of State of Fe-Si Alloys at Super-Earth Core Conditions*, *Sci. Adv.* **4**, eaao5864 (2018).
- [33] F. Coppari, R. F. Smith, J. Wang, M. Millot, D. Kim, J. R. Rygg, S. Hamel, J. H. Eggert, and T. S. Duffy, *Implications of the Iron Oxide Phase Transition on the Interiors of Rocky Exoplanets*, *Nat. Geosci.* **14**, 121 (2021).
- [34] F. Coppari, R. F. Smith, J. H. Eggert, J. Wang, J. R. Rygg, A. Lazicki, J. A. Hawreliak, G. W. Collins, and T. S. Duffy, *Experimental Evidence for a Phase Transition in Magnesium Oxide at Exoplanet Pressures*, *Nat. Geosci.* **6**, 926 (2013).
- [35] D. Kim *et al.*, *Structure and Density of Silicon Carbide to 1.5 TPa and Implications for Extrasolar Planets*, *Nat. Commun.* **13**, 2260 (2022).

- [36] R. G. Kraus, F. Coppari, D. E. Fratanduono, R. F. Smith, A. Lazicki, C. Wehrenberg, J. H. Eggert, J. R. Rygg, and G. W. Collins, *Melting of Tantalum at Multimegabar Pressures on the Nanosecond Timescale*, *Phys. Rev. Lett.* **126**, 255701 (2021).
- [37] J. Wang, F. Coppari, R. F. Smith, J. H. Eggert, A. E. Lazicki, D. E. Fratanduono, J. R. Rygg, T. R. Boehly, G. W. Collins, and T. S. Duffy, *X-Ray Diffraction of Molybdenum under Shock Compression to 450 GPa*, *Phys. Rev. B* **92**, 174114 (2015).
- [38] J.-A. Hernandez *et al.*, *Direct Observation of Shock-Induced Disorder of Enstatite below the Melting Temperature*, *Geophys. Res. Lett.* **47**, e2020GL088887 (2020).
- [39] G. Morard *et al.*, *In Situ X-Ray Diffraction of Silicate Liquids and Glasses under Dynamic and Static Compression to Megabar Pressures*, *Proc. Natl. Acad. Sci. U.S.A.* **117**, 11981 (2020).
- [40] D. Kim *et al.*, *Femtosecond X-Ray Diffraction of Laser-Shocked Forsterite (Mg_2SiO_4) to 122 GPa*, *J. Geophys. Res. Solid Earth* **126**, e2020JB020337 (2021).
- [41] B. Howes, A. Mehra, and A. Maloof, *Three-Dimensional Morphometry of Ooids in Oolites: A New Tool for More Accurate and Precise Paleoenvironmental Interpretation*, *J. Geophys. Res. Earth Surf.* **126**, e2020JF005601 (2021).
- [42] X. Duan *et al.*, *Transparency Measurement of Lithium Fluoride under Laser-Driven Accelerating Shock Loading*, *J. Appl. Phys.* **128**, 015902 (2020).
- [43] F. Coppari, R. F. Smith, D. B. Thorn, J. R. Rygg, D. A. Liedahl, R. G. Kraus, A. Lazicki, M. Millot, and J. H. Eggert, *Optimized X-Ray Sources for X-Ray Diffraction Measurements at the Omega Laser Facility*, *Rev. Sci. Instrum.* **90**, 125113 (2019).
- [44] J. R. Rygg *et al.*, *X-Ray Diffraction at the National Ignition Facility*, *Rev. Sci. Instrum.* **91**, 043902 (2020).
- [45] J. R. Rygg *et al.*, *Powder Diffraction from Solids in the Terapascal Regime*, *Rev. Sci. Instrum.* **83**, 113904 (2012).
- [46] P. M. Celliers, D. K. Bradley, G. W. Collins, D. G. Hicks, T. R. Boehly, and W. J. Armstrong, *Line-Imaging Velocimeter for Shock Diagnostics at the OMEGA Laser Facility*, *Rev. Sci. Instrum.* **75**, 4916 (2004).
- [47] D. E. Fratanduono, T. R. Boehly, M. A. Barrios, D. D. Meyerhofer, J. H. Eggert, R. F. Smith, D. G. Hicks, P. M. Celliers, D. G. Braun, and G. W. Collins, *Refractive Index of Lithium Fluoride Ramp Compressed to 800 GPa*, *J. Appl. Phys.* **109**, 123521 (2011).
- [48] L. E. Kirsch, S. J. Ali, D. E. Fratanduono, R. G. Kraus, D. G. Braun, A. Fernandez-Pañella, R. F. Smith, J. M. McNaney, and J. H. Eggert, *Refractive Index of Lithium Fluoride to 900 Gigapascal and Implications for Dynamic Equation of State Measurements*, *J. Appl. Phys.* **125**, 175901 (2019).
- [49] J. R. Maw, *A Characteristics Code for Analysis of Isentropic Compression Experiments*, *AIP Conf. Proc.* **706**, 1217 (2004).
- [50] S. D. Rothman and J. Maw, *Characteristics Analysis of Isentropic Compression Experiments (ICE)*, *J. Phys. IV (France)* **134**, 745 (2006).
- [51] S. P. Lyon and J. D. Johnson, *Sesame: The Los Alamos National Laboratory Equation of State Database*, Los Alamos National Laboratory, LA-UR-92-3407, 1992.
- [52] D. K. Bradley, J. H. Eggert, R. F. Smith, S. T. Prisbrey, D. G. Hicks, D. G. Braun, J. Biener, A. V. Hamza, R. E. Rudd, and G. W. Collins, *Diamond at 800 GPa*, *Phys. Rev. Lett.* **102**, 075503 (2009).
- [53] F. Coppari, D. E. Fratanduono, M. Millot, R. G. Kraus, A. Lazicki, J. R. Rygg, R. F. Smith, and J. H. Eggert, *X-Ray Diffraction Measurements and Pressure Determination in Nanosecond Compression of Solids up to 600 GPa*, *Phys. Rev. B* **106**, 134105 (2022).
- [54] R. Dutta, B. Kiefer, E. Greenberg, V. B. Prakapenka, and T. S. Duffy, *Ultrahigh-Pressure Behavior of AO_2 ($A = \text{Sn}, \text{Pb}, \text{Hf}$) Compounds*, *J. Phys. Chem. C* **123**, 27735 (2019).
- [55] X. Xia, D. J. Weidner, and H. Zhao, *Equation of State of Brucite: Single-Crystal Brillouin Spectroscopy Study and Polycrystalline Pressure-Volume-Temperature Measurement*, *Am. Mineral.* **83**, 68 (1998).
- [56] M. O. Schoelmerich *et al.*, *Evidence of Shock-Compressed Stishovite above 300 GPa*, *Sci. Rep.* **10**, 10197 (2020).
- [57] A. L. Coleman, M. G. Gorman, R. Briggs, R. S. McWilliams, D. McGonegle, C. A. Bolme, A. E. Gleason, D. E. Fratanduono, R. F. Smith, E. Galtier *et al.*, *Identification of Phase Transitions and Metastability in Dynamically Compressed Antimony Using Ultrafast X-Ray Diffraction*, *Phys. Rev. Lett.* **122**, 255704 (2019).
- [58] Y. Al-Khatatbeh, K. K. M. Lee, and B. Kiefer, *Phase Diagram up to 105 GPa and Mechanical Strength of HfO_2* , *Phys. Rev. B* **82**, 144106 (2010).
- [59] Y. Al-Khatatbeh, K. K. M. Lee, and B. Kiefer, *Phase Relations and Hardness Trends of ZrO_2 Phases at High Pressure*, *Phys. Rev. B* **81**, 214102 (2010).
- [60] J. Haines, J. M. Léger, C. Chateau, and A. S. Pereira, *Structural Evolution of Rutile-Type and CaCl_2 -Type Germanium Dioxide at High Pressure*, *Phys. Chem. Miner.* **27**, 575 (2000).
- [61] S. Ono, T. Tsuchiya, K. Hirose, and Y. Ohishi, *Phase Transition between the CaCl_2 -Type and $\alpha\text{-PbO}_2$ -Type Structures of Germanium Dioxide*, *Phys. Rev. B* **68**, 134108 (2003).
- [62] S. Ono, K. Hirose, N. Nishiyama, and M. Isshiki, *Phase Boundary between Rutile-Type and CaCl_2 -Type Germanium Dioxide Determined by In Situ X-Ray Observations*, *Am. Mineral.* **87**, 99 (2002).
- [63] G. Q. Chen, T. J. Ahrens, and J. K. Knowles, *Effect of Irreversible Phase Change on Shockwave Propagation*, *J. Mech. Phys. Solids* **47**, 763 (1999).
- [64] T. S. Duffy and R. F. Smith, *Ultra-High Pressure Dynamic Compression of Geological Materials*, *Front. Earth. Sci.* **7**, 23 (2019).
- [65] X. Gong, D. N. Polsin, R. Paul, B. J. Henderson, J. H. Eggert, F. Coppari, R. F. Smith, J. R. Rygg, and G. W. Collins, *X-Ray Diffraction of Ramp-Compressed Silicon to 390 GPa*, *Phys. Rev. Lett.* **130**, 076101 (2023).